

# A method for fracture toughness measurement in trabecular bone using computed tomography, image correlation and finite element methods

Liye Yan <sup>a</sup>, Ahmet Cinar<sup>1 a</sup>, Shaocheng Ma <sup>b</sup>, Richard Abel<sup>b</sup>, Ulrich Hansen <sup>c</sup>, Thomas James Marrow <sup>a\*</sup>

a. Department of Materials, University of Oxford, Parks Road, Oxford, OX1 3PH, UK

b. MSk Laboratory, Department of Surgery and Cancer, Faculty of Medicine, Imperial College, London, SW7 2AZ, UK

c. Mechanical Engineering Department, Imperial College London, SW7 2AZ, UK

\*: corresponding author

[James.marrow@materials.ox.ac.uk](mailto:James.marrow@materials.ox.ac.uk)

Tel: +44 1865 273938

Fax: +44 1865 273789

Keywords: Trabecular bone; crack measurement; fracture toughness; computed X-ray tomography; digital volume correlation.

---

<sup>1</sup> Contribution to this work was made whilst a PhD student at University of Sheffield and a Junior Academic Visitor at University of Oxford. Current address: Create Technologies Ltd, Unit 4, Derwent Mills Commercial Park, Wakefield Rd, Cockermouth CA13 0HT, UK

1   **Abstract**

2   The fracture resistance of load-bearing trabecular bone is adversely affected by diseases such  
3   as osteoporosis. However, there are few published measurements of trabecular bone fracture  
4   toughness due to the difficulty of conducting reliable tests in small specimens of this highly  
5   porous material. A new approach is demonstrated that uses digital volume correlation of X-  
6   ray computed tomographs to measure 3D displacement fields in which the crack shape and  
7   size can be objectively identified using a phase congruency analysis. The criteria for crack  
8   propagation, i.e. fracture toughness, can then be derived by finite element simulation, with  
9   knowledge of the elastic properties.

10

## 1 Introduction

Together with cortical bone, trabecular bone contributes to the development of bone fragility with aging (Holzer *et al.*, 2009). Methods are needed to assess the properties of bone in patients, ideally non-destructively and *in vivo* such as micro-indentation (Fyhrie and Christiansen, 2015), but ultimately such measurements need to be calibrated against data obtained by destructive methods that quantify the fracture properties of bone, such as the fracture toughness. The fracture toughness is a material parameter that describes the resistance to crack propagation. In the literature on bone fracture (e.g. (Bonfield, 1987; Norman, Nivargikar and Burr, 1996; Phelps *et al.*, 2000; Lucksanasomboon *et al.*, 2001; Nalla *et al.*, 2005; Ritchie, R.O., 2008)), the fracture toughness is quantified using either the linear elastic fracture mechanics parameter of critical stress intensity factor ( $K_{Ic}$ ) or a critical energy release rate ( $G_c$  or  $J_c$ ). For a linear elastic material, the strain energy release rate,  $G$  can be related via the elastic moduli directly to  $K$ , which describes the crack tip stress field (Irwin, 1957). The  $J$  integral ( $J$ ) allows calculation of the strain energy release rate with non-linear deformation, and it is equivalent to  $G$  under linear elastic conditions. Although the material fracture toughness is independent of specimen size and geometry, incorrect assumptions of the stress and strain fields in the test specimen will lead to inaccurate calculation of the fracture toughness. This can be a particular problem in small or non-standard test specimens, such as those that must be extracted from skeletal bone.

The quite limited literature on the measurement of the fracture toughness of human trabecular bone (Cook and Zioupos, 2009) (Gibson and Ashby, 1999a) (Gibson and Ashby, 1999b) shows that the maximum stress intensity factor that could be sustained prior to fracture increased with the bone density. However, there is little information on how the toughness relates to the pore structure and the intrinsic properties of the bone tissue. To better understand how bone age and condition affect the fracture resistance of trabecular bone, it

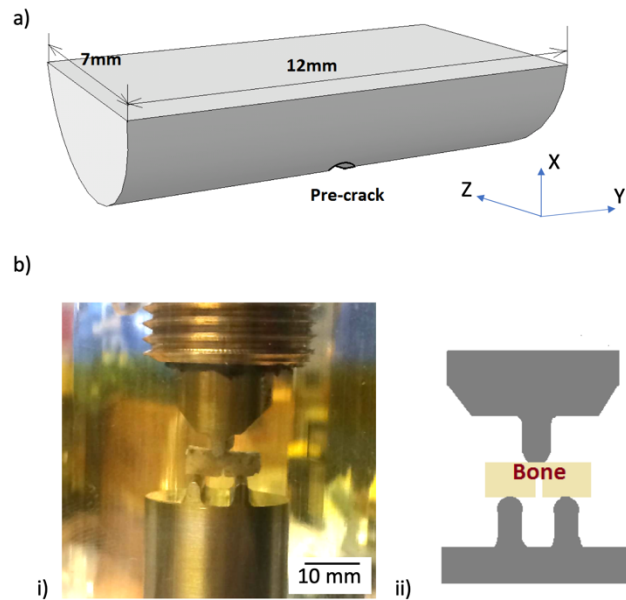
would be useful to have a test method that utilised small test specimens to measure the fracture toughness. Confidence is also needed that such small specimens of highly porous material produce valid fracture toughness data. This is challenging, firstly due to difficulties in determining the crack geometry in a highly porous material, and secondly because one needs to have reliable knowledge of the deformation of the small test specimen in order to calculate the strain energy release rate for fracture propagation.

This study aims to develop a method to evaluate the fracture toughness of trabecular bone using small test specimens. An example analysis is presented of an in situ fracture test, observed by synchrotron X-ray computed tomography. An important consideration is how the crack geometry can be defined and visualised in the porous trabecular bone, in order to determine the dimensions and effective shape. This is done using gradients of the three-dimensional displacement field that is measured by digital volume correlation of tomographs. Knowledge of the displacement field around the crack also allows a calculation of the strain energy release rate at which the crack becomes unstable and this is compared with the expected fracture toughness of trabecular bone.

## **2 Materials and methods**

The data were obtained during an experiment (beamtime allocation EE 11204-1) conducted in hutch 1 on beamline I12 at the Diamond Light Source, UK. The bone specimen was prepared from the trabecular chiasma of a human femoral head. A core was obtained using a low speed drill under constant irrigation then sectioned into a semi-cylindrical shape with dimensions of 12 mm length x 7 mm thickness x 3.5 mm width (Figure 1a). A sharp notch with a depth of approximately 0.15 mm was introduced into the curved surface using a razor blade. The specimen was loaded under displacement control using a three-point bending test rig (Figure 1b) and was observed by computed tomography at intervals as the load was

- 1 increased. The bending rig was mounted within a purpose-built X-ray and optically
- 2 transparent loading rig<sup>2</sup>, and employed three fixed rollers with a 1 mm radius of curvature.
- 3 Water was sprayed onto the sample to moisten it before the tomography scans commenced.



4  
5 *Figure 1: Three point bending test of miniature trabecular bone specimen: (a) Specimen*  
6 *geometry; (b) Three-point bending test on pre-notched bone (i) image from experiment*  
7 *ii) schematic arrangement.*

8 The tomographs were recorded under static load at 5 N intervals until the specimen failed at  
9 37 N, beginning from a pre-load of 5 N. Each observation comprised a total of 3000  
10 projections, over a 180° rotation, with an exposure time of 0.2 s per projection using the  
11 module 3 optics at a monochromatic beam energy beam of 112.6 KeV (0.1% beam energy

---

<sup>2</sup> Loaned from the University of Birmingham, the digitally-controlled loading rig was equipped with a 1 kN load cell (1 N precision); the balancing tensile load was taken by a polycarbonate tube (internal diameter 50 mm, external diameter 60 mm) that surrounds the specimen and is X-ray and optically transparent.

resolution). The flux density at this energy and bandwidth in hutch 1 was  $2.34 \times 10^{10}$  photons  $\text{s}^{-1} \text{mm}^{-2}$ . The scan time at each load was approximately 10 minutes.

The tomography reconstruction used the standard attenuation contrast back-projection algorithms and pre/post processing methods to reduce noise and image artefacts that were available on the I12 beamline. Each tomograph comprised a volume of  $\sim 7 \times 7 \times 7 \text{ mm}^3$ , centred at the pre-notch, at a voxel resolution of  $3.25 \mu\text{m}^3$ . Visualisation of the tomography data was done using ImageJ<sup>3</sup> and Avizo Fire (Version 9.7). The digital volume correlation (DVC) analysis to measure the full field displacements employed the LaVision DaVis software (version 8.4.0) using the FFT algorithm with a  $64 \times 64 \times 64$  voxel subset at 75% overlap applied to tomographs with the pre-load as the reference and obtained vectors with correlation coefficient less than 0.4 were discarded. Prior to the DVC analysis, the 32 bit tomographs were down-sampled to 8 bit using ImageJ, choosing a 0-256 grey level range to maximise contrast in the bone structure with 3D Gaussian blur filter applied to minimize data noise.

### 3 Results

Tomography (Figure 2a) reveals the porous structure of the trabecular bone; the example in the figure is observed at 35 N. The major constituents of the microstructure can be identified by their relative X-ray attenuation; bone matrix (light); soft tissue (darker) and open porosity (darkest, and equivalent to the surrounding air). However, the razor cut pre-notch and crack are difficult to identify in the orthogonal sections (Figure 2b to d) as the crack has low contrast due to the small opening; its location is indicated by white dashed ellipses.

---

<sup>3</sup> Schneider, C.A., Rasband, W.S., Eliceiri, K.W. "NIH Image to ImageJ: 25 years of image analysis". Nature Methods 9, 671-675, 2012.

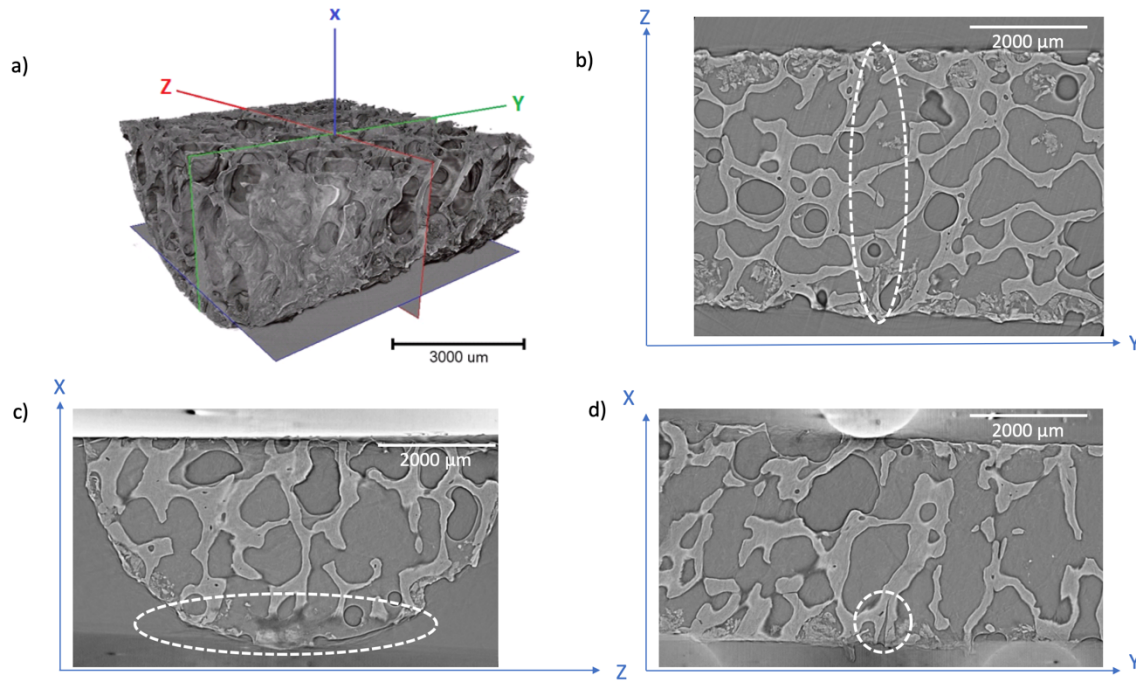


Figure 2: Tomographs of trabecular bone under 35 N load. (a) 3D volume of bone; (b) y-z plane view; (c) x-z plane view; (d) x-y plane view. The crack is within the white dashed ellipse.

The crack is made more apparent by observing its effect on the displacement field, which is obtained by digital volume correlation. Figure 3a shows sections of the displacement field measured at 35 N. There is a relative opening ( $U_y$ ) of approximately 20 μm in the y-direction, parallel to the applied bending stress, compared to which the other orthogonal displacements across the crack are insignificant. The effect of the crack and notch can then be visualised using the maximum normal 3D strain (Figure 3b). This measures the local gradient of the displacement field, which is maximised at the discontinuity of the crack. Noise in the displacement field also creates local strains, but by selecting a sufficient threshold strain (0.002) above the background level of noise, the evolution of the crack can be visualised with increasing load (Figure 4a). The crack shape was also visualised using a 3D edge detection algorithm that employs phase congruency (Cinar *et al.*, 2017) to identify the discontinuity in the displacement field this is caused by the crack. This provides a

visualisation of the crack's evolution that is similar to the maximum normal 3D strain, but with a threshold criterion that is less subjective and less sensitive to noise in the displacement field data (Figure 4b). There are no displacement data obtained from within the soft bone tissue or the pores, hence due to the significant heterogeneity of the porous bone both the visualisations using strain and 3D phase congruency present a non-uniform crack front that depends on the spatial distribution of the bone matrix.

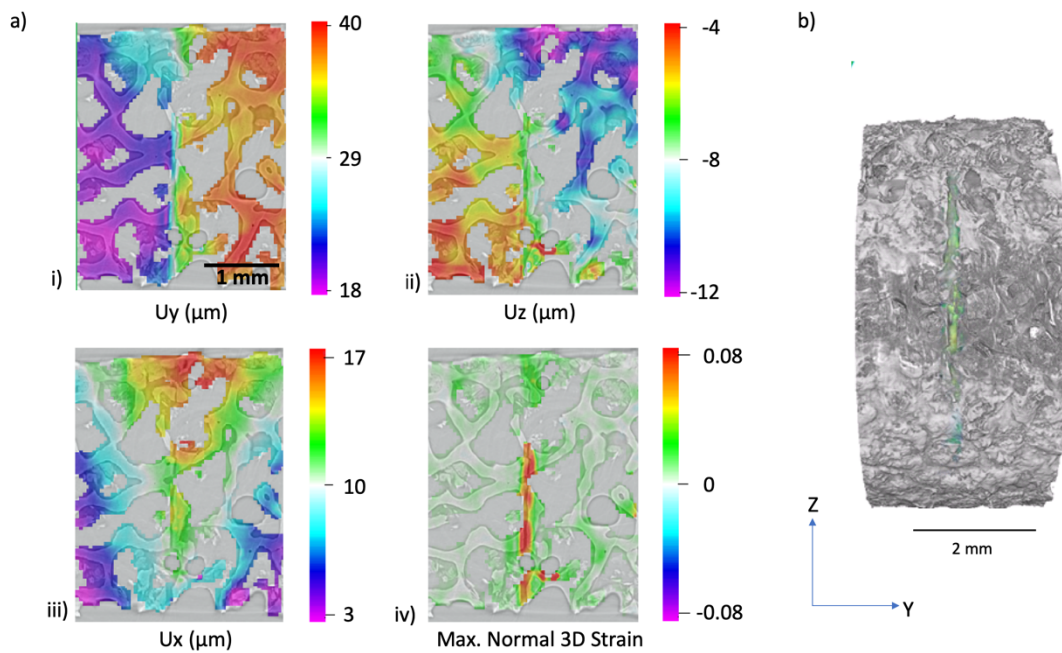


Figure 3: (a) The displacement field, measured by DVC at a load of 35 N, presented on selected y-z plane near the specimen centre: i) y displacement ( $U_y$ ); ii) z displacement ( $U_z$ ); iii) x displacement ( $U_x$ ); and iv) Maximum Normal 3D Strain; (b) crack segmentation using on the maximum normal 3D strain, visualised with a 3D tomograph of the specimen.



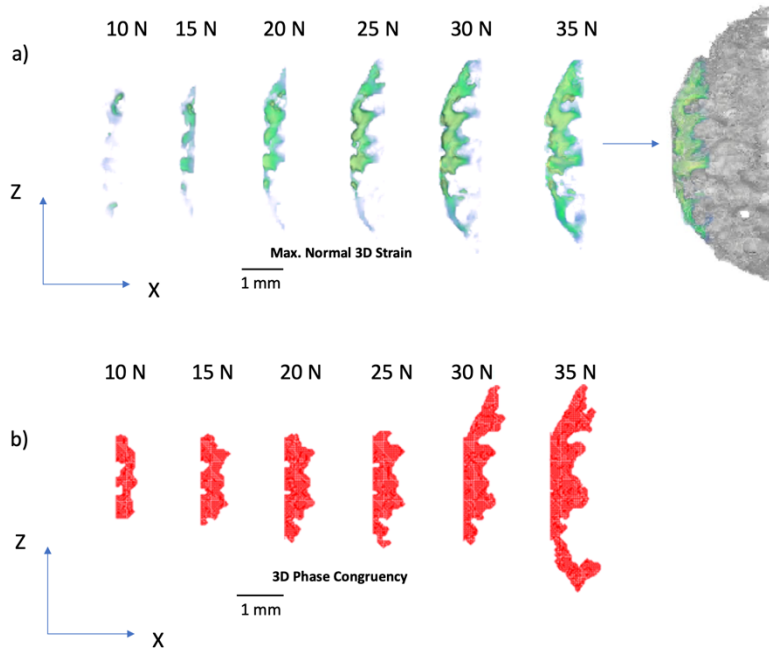
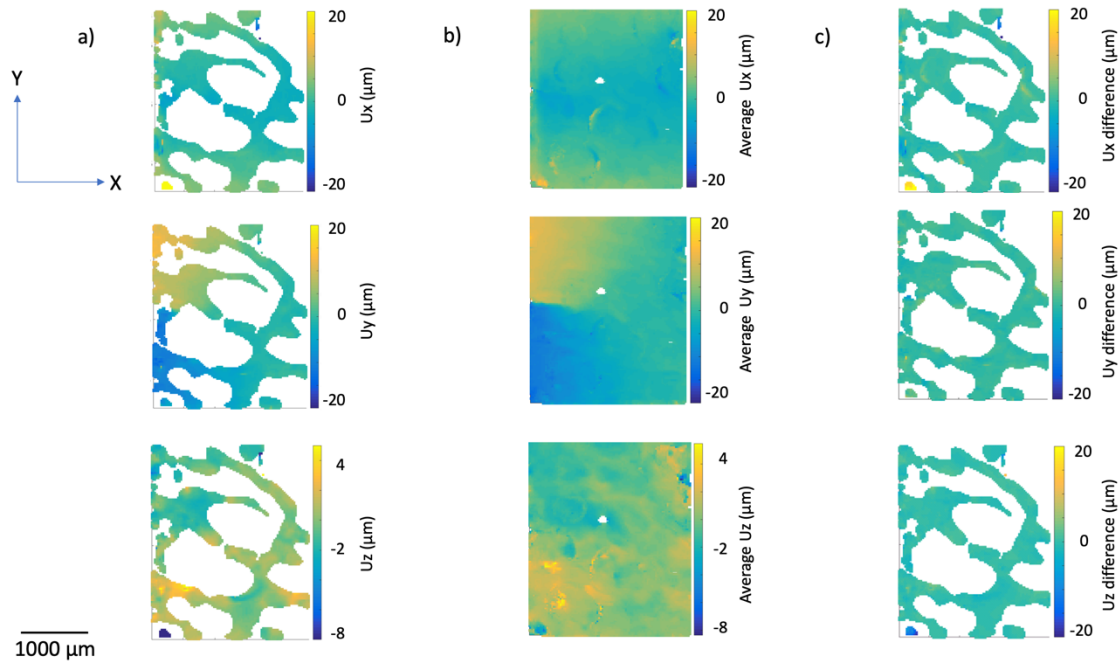


Figure 4: The observed evolution of the crack, projected in the x-z plane, by analysis of the displacement field: (a) Crack segmentation using maximum normal 3D strain; (b) Crack segmentation using 3D phase congruency.

To address this heterogeneity, the 3D displacement field (after removal of rigid body translations and rotations) was transformed to an equivalent 2D representation parallel to the x-y plane by averaging the displacements at each (x,y) coordinate along the z-axis. Only those points with a measured displacement vector were included; a near-continuous displacement field was obtained as there was at least one measurement at almost every coordinate. To check that the 3D data is adequately represented by this 2D field, the differences between the original and averaged displacement fields were assessed. The displacement components in a representative section of the original 3D displacement field for a plane that is close to the specimen centre are shown in Figure 5a, while Figure 5b shows the averaged 2D values, in which there is a clear discontinuity in the averaged  $U_y$  field due to the crack. The difference between the original and averaged fields is negligible (Figure 5c), except in a few localised regions. Observations in other slices through the data were similar,

- 1 confirming that the deformation of this specimen in flexural loading can be considered as
- 2 essentially 2D.



3  
4 *Figure 5: (a) Original displacement fields on a central x-y plane. (b) Averaged displacement*  
5 *fields. (c) Differences between original and averaged displacement fields.*

6 The evolution of the crack length was then assessed by analysis of the 2D phase congruency  
7 values (Cinar *et al.*, 2017), calculated for the  $U_y$  field. First, missing data (NaN data) in the  
8 averaged displacement field (Figure 6a) were interpolated using the known values to obtain a  
9 filled displacement field. An outlier removal method was then employed (Westerweel and  
10 Scarano, 2005). The crack could then be readily identified and measured as a linear feature  
11 with high phase congruency (Figure 6b). The obtained crack lengths are summarised in  
12 Figure 7, together with averaged values measured at different  $z$  positions at equally spaced  
13 intervals for the 3D strain and 3D phase congruency visualisations (Figure 4). The crack  
14 lengths measured using 2D and 3D phase congruency show a similar trend of increasing  
15 length with increasing load; slightly higher values are obtained by the 2D method. The  
16 measurement uncertainty in the 2D phase congruency method arises from the data intervals in

the displacement field and so depends on the DVC subset size and overlap. There is a larger uncertainty for the 3D strain and 3D phase congruency, calculated as the standard deviation of the measurements, and this is quite significant for the 3D strain segmentation at low load as the strain values are low and are affected by noise in the DVC data. The 3D phase congruency is less influenced by this noise. The 2D phase congruency provides a quite consistent measure of the maximum extent of the crack.

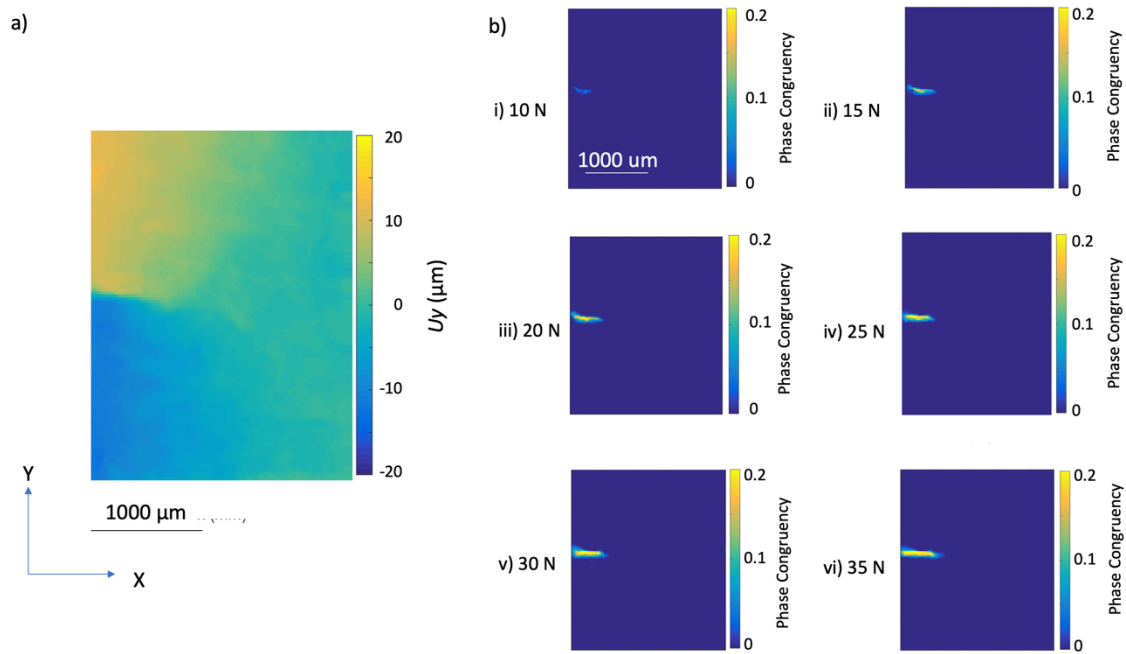


Figure 6: (a) Map of the averaged displacements,  $U_y$ , in the  $x$ - $y$  plane at a load of 35 N; (b) Maps of the 2D phase congruency value (Cinar et al., 2017) with increasing loads, identifying the development of the crack.

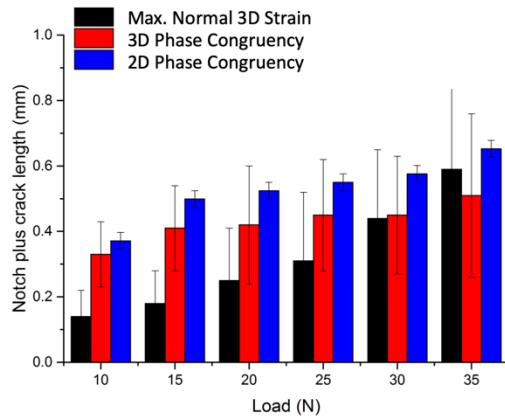


Figure 7: Measured crack lengths (including notch) at different loads, obtained by thresholding segmentation of the maximum normal 3D strain field, and 3D and 2D phase congruency analysis of displacement fields.

#### 4 Analysis of the $J$ integral and stress intensity factor

The  $J$ -integral, which describes the strain energy release rate, can be calculated directly from the stress and strain fields of a crack as a contour path integral. Theoretically, the  $J$ -integral is contour independent and the contour to evaluate the strain energy release rate of a crack must start and end from a traction-free surface, such as the crack surface. The  $J$ -integral can be formulated as a surface or area integral, and this is convenient to implement in finite element analyses. Hence methods to directly evaluate the  $J$ -integral from the measured crack fields have been developed such as the JMAN method (Barhli *et al.*, 2017) (Becker *et al.*, 2012) (Becker, Marrow and Tait, 2011), which implements the area integral with DIC measurements. The application of other integrals with full-field displacement data can be found in the literature (Moutou and Claudiu, 2014). These methods do not rely on fitting a presumed field (e.g. the Williams' series) and the calculation is quite robust to uncertainty in the crack tip position.

Having determined the average 2D displacement field and the position of the crack tip based on 2D segmented crack, the JMAN method (Barhli *et al.*, 2017) was used for the  $J$ -integral calculation. The displacements provide the strain field, so values of Poisson's ratio and Young's modulus are required for the calculation of the stress field and eventually the  $J$ -integral. The Poisson's ratio is taken to be 0.3, which is a value commonly assumed for trabecular bone (An and Robert, 2000) (Kabel *et al.*, 1999) (Colabella *et al.*, 2017). The elastic modulus of trabecular bone was taken as 0.26 GPa, derived from tensile test data (Ma *et al.*, 2017) and assumed to be constant and homogeneous.

Implementing the JMAN method gave a field of approximately 11000 regular square grid elements, the centres of which are represented by the displacements. The crack was masked, and an outer contour and an inner contour were manually selected (Figure 8a). The  $J$ -integral was evaluated at multiple contours between these, using the element-based virtual crack extension formulation (Parks, 1977). The calculation assumes a plane-strain condition, as the DVC data show there is no significant strain in the  $z$  direction. The evolution of the  $J$  integral with increasing outer contour size is shown in Figure 8b for each load. Scattered results are obtained for the contours near to the masked region, as these are more affected by data noise in the displacement field. However, the  $J$ -integral value tends to converge to a constant plateau with increasing contour number. The obtained  $J$ -integral is presented against load in Figure 8c; the standard deviation of the values in the plateau is used to assess the uncertainty. The  $J$ -integral value increases with increasing load. From the  $J$  integral, the applied stress intensity factor  $K$  was calculated with the assumption of plane strain linear elasticity (Irwin, 1957), finding a quite linear relation between  $K$  and load (Figure 8d).

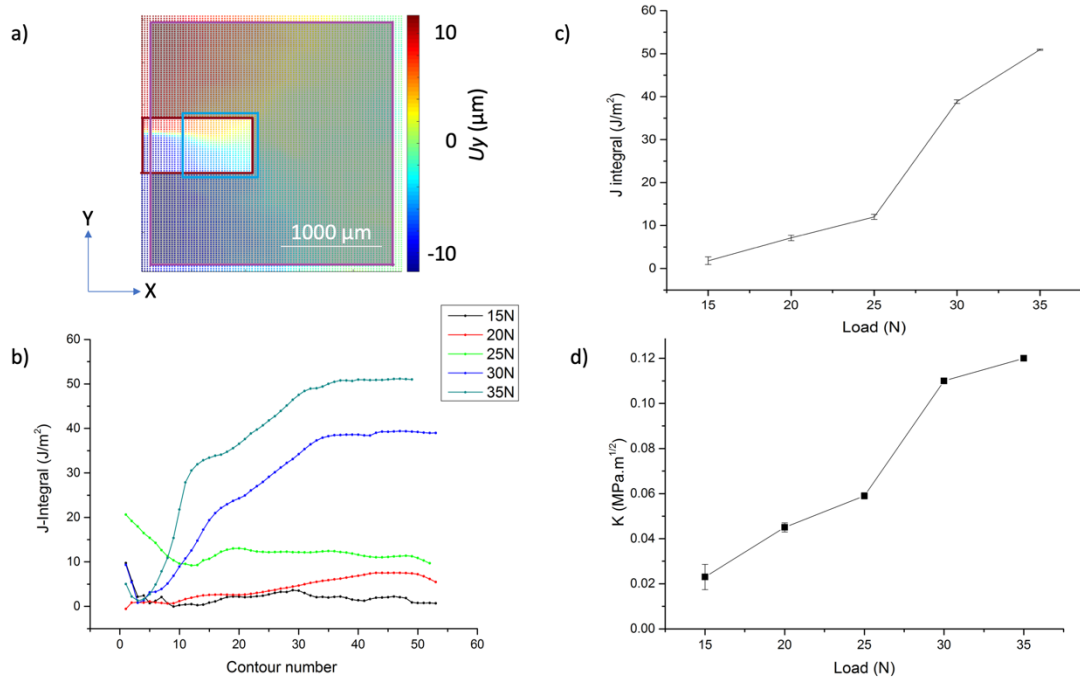


Figure 8: (a) Selected inner and outer contours and masked region of the crack for JMAN analysis of the J-integral at 35 N load. (b) The J-integral with increasing contour number at different load. (c) The plateau value of J-integral vs. load. (d) The stress intensity factor,  $K$ , obtained from the plateau J-integral, vs. load.

## 5 Discussion

Phase congruency analysis of 3D displacement fields provide a less subjective segmentation of the crack than the maximum 3D strain, but both are affected by the heterogeneity of the available data in the highly porous trabecular bone microstructure. The compression of 3D data to 2D provides a representative description of the deformation of the specimen, allowing the effective crack length to be identified and measured using phase congruency of the displacement field. This method may have wider application for detection and characterisation of cracks in other porous solids.

The crack length did not change significantly with increasing load as failure was approached, and the critical stress intensity factor  $K_c$  was estimated by linear extrapolation of the observed

trend between stress intensity factor and load (Figure 8d) between 30 N and 35 N to the failure load of 37 N to obtain a value of  $0.14 \pm 0.04 \text{ MPa m}^{1/2}$ . To assess the reliability of this measurement, it may be compared with independent measurement from the literature. Data on the fracture toughness of trabecular bone are limited, but it has been shown that the fracture toughness of cancellous bone depends on the bone density (Cook and Zioupos, 2009).

$$\log K_c = -0.21 + 1.53 \log \rho_{app} \quad (1)$$

where  $K_c$  ( $\text{MPa m}^{1/2}$ ) is the critical stress intensity factor for crack propagation and  $\rho_{app}$  is the apparent density ( $\text{g cm}^{-3}$ ) (Cook and Zioupos, 2009). The density of the studied trabecular bone is not known, but a recent study measured elastic moduli of trabecular bone between 0.1-0.4 GPa (Ma *et al.*, 2017), with an average of 0.26 GPa. A relation between the elastic modulus and density of trabecular bone is reported in the literature (Keaveny *et al.*, 1994),

$$E_{app} = 8420\rho_{app} - 2430 \quad (2)$$

where  $E_{app}$  is the apparent elastic modulus (MPa) and  $\rho_{app}$  is the apparent density ( $\text{g/cm}^3$ ). Hence from equation (2) the density of the trabecular bone with modulus 0.26 GPa is estimated to be  $0.32 \text{ g cm}^{-3}$  and from equation (1) its fracture toughness is estimated to be  $0.11 \text{ MPa m}^{1/2}$ . This is in fair agreement with the value obtained from the JMAN analysis of the displacement field.

It is important to consider whether the synchrotron irradiation exposure has a possible influence on the properties of the inspected sample. Several studies have investigated the effects of micro-CT and synchrotron radiation on bone tissue mechanics. (Barth *et al.*, 2010, 2011) exposed bone samples to 0, 0.05, 70, 210 and 630 kGy doses during synchrotron micro-CT experiments and reported that doses over 70 kGy were associated with reduced

strength and toughness. (Fernández *et al.*, 2018) used synchrotron X-ray micro-CT and DVC to study trabecular bone mechanics, and found that there was no measurable damage or effect on bone plasticity for low irradiation doses ( $\sim 33$  kGy), although there was degradation in data quality that suggested some effect on the microstructure. Recently (Tay, 2020) tested the effects of X-Ray irradiation on tissue, fibril and mineral strains in bone samples of similar dimensions to those in this study using the I22 diffraction beamline at the Diamond Light Source (Didcot, UK). With increasing dosage from 0.0003 kGy to 30 kGy the tissue, fibril and mineral strains did not change significantly.

In this work, the dose experienced by the specimen was estimated following the method of (Barth *et al.*, 2010, 2011) with a mass attenuation coefficient at 112.6 keV of  $0.176 \text{ cm}^2 \text{ g}^{-1}$  (Hubbell and Seltzer, 1995) and density  $0.32 \text{ g cm}^{-3}$ . Simplifying with the conservative assumption of cubic specimen dimensions of 3.5 mm, the total absorption of the incident flux by the specimen was 2%. Hence the total irradiated dose per tomograph was less than 2.5 kGy (including attenuation by the loading stage of  $\sim 9\%$ ). Due to the use of monochromatic and high energy X-rays, which have significantly lower absorption than lower energy X-rays, the estimated total dose for the sample examined in this study was less than 15 kGy, so the synchrotron X-ray irradiation is not expected to have had any significant effect on the structure or properties of the sample.

The objective of the work was to demonstrate that a representative crack and crack strain field could be extracted from a highly porous test specimen of trabecular bone, and this could then be used to estimate the critical condition at the crack tip at the onset of fracture propagation. A simplistic and approximate analysis has been presented, which assumed homogeneous linear elastic properties with a magnitude representative of trabecular bone. Nonetheless, the critical stress intensity factor obtained is a good estimate of the expected



fracture toughness of low density (i.e. low volume fraction) trabecular bone. This analysis does not depend on the geometry of the test specimen, nor measurement of the applied load. In principle, the elastic modulus of the tested specimen could be extracted using the DVC measured displacement field, for instance by calculation of the strain gradient to correlate with the applied bending moment (Wan *et al.*, 2018), or more accurately by injection of the measured displacement field into a finite element simulation of the test specimen (Ramsay, 2013). Non-linear elastic properties can also be applied, using a development of the JMAN method (Barhli, 2017), and these could be measured via *in situ* tomography observations during successive unloading (Marrow *et al.*, 2016). The presented method could then be used to obtain the fracture toughness of small specimens of highly porous trabecular bone, and this would allow more detailed studies, such as the effects of bone ageing, osteoporosis and subsequent medical treatments on bone properties (Boughton *et al.*, 2019). Such studies are increasingly important as the material basis for bone strength and fragility and role of microcracks in fragility fractures is becoming apparent (Jin *et al.*, 2017) (Ma *et al.*, 2017).

## 6 Conclusion

A novel method has been presented to obtain the fracture toughness using *in situ* observations of small specimens of a highly porous material, trabecular bone. The position of the crack tip that developed in highly porous trabecular bone have been measured by the application of phase congruency to displacement fields that were calculated by digital volume correlation of computed X-ray tomographs. Linear elastic finite analysis of the deformation field around the crack tip provided a good estimate of the critical stress intensity factor for crack propagation.

## **7 Acknowledgements**

The authors acknowledge support from the MSk Lab, Department of Surgery and Cancer, Imperial College, London. The use of facilities funded by EPSRC Grant EP/M02833X/1 “University of Oxford: experimental equipment upgrade” is gratefully acknowledged. The authors are grateful for funding provided by the National Institute for Health Research (NIHR) Imperial BRC, The Royal College of Surgeons of England, The Dunhill Medical Trust and the Michael Uren Foundation. Birmingham University (Prof. Brian Connolly) is acknowledged for the loan of the loading rig, which was provided via EPSRC Grant (EP/H025286/1: Long Term, In Situ Material Degradation Studies Utilizing High Resolution Laboratory X-ray Tomography). Beamtime at the Diamond Light Source, UK, was awarded as experiment EE11204-1. We are grateful to Dr Thomas Connolly for providing data on the photon flux density in hutch 1 at beamline I12.

This study received ethical approval (Imperial Tissue Bank number R13004a, Wales Research Ethics Committee number 12/WA/0196) and all patients gave written, informed consent for the use of their tissue for research. The authors would like to thank the patients for their donation.

## 8 References

- An, Y. H. and Robert, A. D. (eds) (2000) *Mechanical testing of bone and the bone-implant interface*. United states of America: CRC Press. doi: 10.1201/9781420073560.
- Barhli, S. M. (2017) *Advanced quantitative analysis of crack fields, observed by 2D and 3D image correlation, volume correlation and diffraction mapping*. University of Oxford. Available at: <https://ora.ox.ac.uk/objects/uuid:d6240241-8a1e-4a8e-aff0-4a2ef14b0da7>.
- Barhli, S. M. *et al.* (2017) 'J-Integral Calculation by Finite Element Processing of Measured Full-Field Surface Displacements', *Experimental Mechanics*, 57(6), pp. 997–1009. doi: 10.1007/s11340-017-0275-1.
- Barth, H. D. *et al.* (2010) 'On the effect of X-ray irradiation on the deformation and fracture behavior of human cortical bone', *Bone*, 46(6), pp. 1475–1485. doi: <https://doi.org/10.1016/j.bone.2010.02.025>.
- Barth, H. D. *et al.* (2011) 'Characterization of the effects of x-ray irradiation on the hierarchical structure and mechanical properties of human cortical bone', *Biomaterials*, 32(34), pp. 8892–8904. doi: <https://doi.org/10.1016/j.biomaterials.2011.08.013>.
- Becker, T. H. *et al.* (2012) 'An approach to calculate the J-integral by digital image correlation displacement field measurement', *Fatigue and Fracture of Engineering Materials and Structures*. Department of Mechanical and Mechatronic Engineering, University of Stellenbosch, Stellenbosch 7600, pp. 971–984. doi: 10.1111/j.1460-2695.2012.01685.x.
- Becker, T. H., Marrow, T. J. and Tait, R. B. (2011) 'Damage, crack growth and fracture characteristics of nuclear grade graphite using the Double Torsion technique', *Journal of Nuclear Materials*. University of Cape Town, University of Manchester, School of Materials, Manchester M13 9PL, United Kingdom, 414(1), pp. 32–43. doi: 10.1016/j.jnucmat.2011.04.058.
- Bonfield, W. (1987) 'Advances in the fracture mechanics of cortical bone', *Journal of Biomechanics*, 20(11–12), pp. 1071–1081. doi: 10.1016/0021-9290(87)90025-X.
- Boughton, O. R. *et al.* (2019) 'Computed tomography porosity and spherical indentation for determining cortical bone millimetre-scale mechanical properties', *Scientific Reports*, 9(1), p. 7416. doi: 10.1038/s41598-019-43686-6.
- Cinar, A. F. *et al.* (2017) 'An autonomous surface discontinuity detection and quantification method by digital image correlation and phase congruency', *Optics and Lasers in Engineering*, 96, pp. 94–106. doi: 10.1016/j.optlaseng.2017.04.010.
- Colabella, L. *et al.* (2017) 'Calculation of cancellous bone elastic properties with the polarization-based FFT iterative scheme', *International Journal for Numerical Methods in Biomedical Engineering*, 33(11), pp. 1–16. doi: 10.1002/cnm.2879.
- Cook, R. B. and Zioupos, P. (2009) 'The fracture toughness of cancellous bone', *Journal of Biomechanics*. Elsevier, 42(13), pp. 2054–2060. doi: 10.1016/j.jbiomech.2009.06.001.
- Fernández, M. P. *et al.* (2018) 'Effect of SR-microCT radiation on the mechanical integrity of trabecular bone using in situ mechanical testing and digital volume correlation', *Journal of the Mechanical Behavior of Biomedical Materials*, 88, pp. 109–119. doi: <https://doi.org/10.1016/j.jmbbm.2018.08.012>.
- Fyhrie, D. P. and Christiansen, B. A. (2015) 'Bone Material Properties and Skeletal Fragility

- 1 Bone Material Properties and Skeletal Fragility', *Calcified Tissue International*. Springer US,  
2 (May). doi: 10.1007/s00223-015-9997-1.
- 3 Gibson, L. J. and Ashby, M. F. (1999a) 'Chapter 10: Wood', in *Cellular solids: Structure and*  
4 *properties, second edition*. Cambridge University Press, pp. 387–428.
- 5 Gibson, L. J. and Ashby, M. F. (1999b) 'Chapter 11: Cancellous bone', in *Cellular solids:*  
6 *Structure and properties, second edition*. Cambridge University Press, pp. 429–452.
- 7 Holzer, G. *et al.* (2009) 'Hip fractures and the contribution of cortical versus trabecular bone  
8 to femoral neck strength', *Journal of Bone and Mineral Research*, 24(3), pp. 468–474. doi:  
9 10.1359/jbmr.081108.
- 10 Hubbell, J. H. and Seltzer, S. M. (1995) *Tables of x-ray mass attenuation coefficients and*  
11 *mass energy-absorption coefficients 1 keV to 20 MeV for elements z = 1 to 92 and 48*  
12 *additional substances of dosimetric interest*. United States. Available at:  
13 <https://www.osti.gov/servlets/purl/76335>.
- 14 Irwin, G. R. (1957) 'Analysis of Stresses and Strains Near the End of a Crack Traversing a  
15 Plate', *J. Appl. Mech.*
- 16 Jin, A. *et al.* (2017) 'The effect of long-term bisphosphonate therapy on trabecular bone  
17 strength and microcrack density', *Bone and Joint Research*, 6, pp. 602–609. doi:  
18 10.1302/2046-3758.610.BJR-2016-0321.R1.
- 19 Kabel, J. *et al.* (1999) 'Constitutive relationships of fabric, density, and elastic properties in  
20 cancellous bone architecture', *Bone*, 25(4), pp. 481–486. doi: 10.1016/S8756-  
21 3282(99)00190-8.
- 22 Keaveny, T. M. *et al.* (1994) 'Trabecular bone exhibits fully linear elastic behaviour and  
23 yields at low strains', *Biomechanics*, 27(9), pp. 1127–1136.
- 24 Lucksanasombool, P. *et al.* (2001) 'Fracture toughness of bovine bone: Influence of  
25 orientation and storage media', *Biomaterials*, 22(23), pp. 3127–3132. doi: 10.1016/S0142-  
26 9612(01)00062-X.
- 27 Ma, S. *et al.* (2017) 'Long-term effects of bisphosphonate therapy : perforations , microcracks  
28 and mechanical properties', *Nature Publishing Group*. Nature Publishing Group, (November  
29 2016), pp. 1–10. doi: 10.1038/srep43399.
- 30 Marrow, T. J. *et al.* (2016) 'In situ measurement of the strains within a mechanically loaded  
31 polygranular graphite', *Carbon*, 96, pp. 285–302. doi: 10.1016/j.carbon.2015.09.058.
- 32 Moutou, R. and Claudiu, P. (2014) 'Characterization of a cracked specimen with full-field  
33 measurements : direct determination of the crack tip', *Int J Fract*, 187(1), pp. 109–121. doi:  
34 10.1007/s10704-013-9921-5.
- 35 Nalla, R. K. *et al.* (2005) 'Mechanistic aspects of fracture and R-curve behavior in human  
36 cortical bone.', *Biomaterials*, 26(2), pp. 217–31. doi: 10.1016/j.biomaterials.2004.02.017.
- 37 Norman, T. L., Nivargikar, S. V. and Burr, D. B. (1996) 'Resistance to crack growth in  
38 human cortical bone is greater in shear than in tension', *Journal of Biomechanics*, 29(8), pp.  
39 1023–1031. doi: 10.1016/0021-9290(96)00009-7.
- 40 Parks, D. M. (1977) 'The virtual crack extension method for nonlinear material behavior',  
41 *Computer Methods in Applied Mechanics and Engineering*, 12(3), pp. 353–364. doi:  
42 [https://doi.org/10.1016/0045-7825\(77\)90023-8](https://doi.org/10.1016/0045-7825(77)90023-8).

- 1 Phelps, J. B. *et al.* (2000) 'Microstructural heterogeneity and the fracture toughness of bone',  
2 *Journal of biomedical materials research*, 51(September), pp. 735–741. doi: 10.1002/1097-  
3 4636(20000915)51.
- 4 Ramsay, P. (2013) 'Mechanical Property Measurements on AGR Core Graphite Using  
5 Electronic Speckle Pattern Interferometry', in *Modelling and Measuring Reactor Core*  
6 *Graphite Properties and Performance*. The Royal Society of Chemistry, pp. 61–68. doi:  
7 10.1039/9781849735179-00061.
- 8 Ritchie, R.O., et al (2008) 'Measurement of the toughness of bone: A tutorial with special  
9 reference to small animal studies', *Bone*, 43(5), pp. 798–812. doi: 10.1111/j.1743-  
10 6109.2008.01122.x.Endothelial.
- 11 Tay, T. J. H. (2020) *The effects of synchrotron x-ray radiation. Changes in bone's*  
12 *nanostructure associated with bone fragility & bisphosphonate treatment*. Imperial College  
13 London.
- 14 Wan, F. *et al.* (2018) 'Damage development during flexural loading of a 5-directional braided  
15 C/C-SiC composite, characterized by X-ray tomography and digital volume correlation',  
16 *Ceramics International*. Elsevier. doi: 10.1016/J.CERAMINT.2018.12.020.
- 17 Westerweel, J. and Scarano, F. (2005) 'Universal outlier detection for PIV data', *Experiments*  
18 *in Fluids*, 39(6), pp. 1096–1100. doi: 10.1007/s00348-005-0016-6.

## 9 Figure Captions

Figure 1: Three point bending test of miniature trabecular bone specimen: (a) Specimen geometry; (b) Three-point bending test on pre-notched bone (i) image from experiment ii) schematic arrangement.

Figure 2: Tomographs of trabecular bone under 35 N load. (a) 3D volume of bone; (b) y-z plane view; (c) x-z plane view; (d) x-y plane view. The crack is within the white dashed ellipse.

Figure 3: (a) The displacement field, measured by DVC at a load of 35 N, presented on selected y-z plane near the specimen centre: i) y displacement ( $U_y$ ); ii) z displacement ( $U_z$ ); iii) x displacement ( $U_x$ ); and iv) Maximum Normal 3D Strain; (b) crack segmentation using on the maximum normal 3D strain, visualised with a 3D tomograph of the specimen.

Figure 4: The observed evolution of the crack, projected in the x-z plane, by analysis of the displacement field: (a) Crack segmentation using maximum normal 3D strain; (b) Crack segmentation using 3D phase congruency.

Figure 5: (a) Original displacement fields on a central x-y plane. (b) Averaged displacement fields. (c) Differences between original and averaged displacement fields.

Figure 6: (a) Map of the averaged displacements,  $U_y$ , in the x-y plane at a load of 35 N; (b) Maps of the 2D phase congruency value (Cinar et al., 2017) with increasing loads, identifying the development of the crack.

Figure 7: Measured crack lengths (including notch) at different loads, obtained by thresholding segmentation of the maximum normal 3D strain field, and 3D and 2D phase congruency analysis of displacement fields.

- 1 *Figure 8: (a) Selected inner and outer contours and masked region of the crack for JMAN*
- 2 *analysis of the J-integral at 35 N load. (b) The J-integral with increasing contour number at*
- 3 *different load. (c) The plateau value of J-integral vs. load. (d) The stress intensity factor, K,*
- 4 *obtained from the plateau J-integral, vs. load.*